LAWRENCE
LIVERMORE
NATIONAL
LABORATORY

LLNL-JRNL-812443

Transformation of Ferrihydrite to Geothite and the Fate of Plutonium

E. Balboni, K. F. Smith, L. Moreau, T. T. Li, C. Booth, A. B. Kersting, M. Zavarin, M. Maloubier

July 13, 2020

Earth and Space Chemistry

Disclaimer

Transformation of ferrihydrite to goethite and the fate of plutonium

Enrica Balboni[1], Kurt F. Smith[2], Liane M. Moreau [2], Tian T. Li[3], Melody Maloubier[4]†, Corwin H. Booth[2], Annie B. Kersting[1], Mavrik Zavarin[1]*

[1] Glenn T. Seaborg Institute, Physical & Life Sciences Directorate, Lawrence Livermore National Laboratory, P.O. Box 808, Livermore, CA 94550, USA

[2] Chemical Sciences Division, Lawrence Berkeley National Laboratory, Berkeley, CA 94720, USA

[3] Material Science division, Physical & Life Sciences Directorate, Lawrence Livermore National Laboratory, Livermore, CA 94550, USA

[4] Department of Environmental Engineering & Earth Sciences, Clemson University, Clemson, SC, 29634, USA[1]

* Email: balboni1@llnl.gov; Phone: 925-422-4833.

† Currently at IJCLab (Laboratoire de Physique des des deux infinis Irène Joliot-Curie - UMR 9012)

KEYWORDS: Ferrihydrite, goethite, plutonium, extended x-ray absorption fine structure spectroscopy

Understanding interactions between plutonium and iron (oxy)hydroxide minerals is necessary to gain a predictive understanding of plutonium environmental mobility and evaluating long-term performance of nuclear waste repositories. We investigated the fate of plutonium during the formation of ferrihydrite and its subsequent transformation to goethite. Ferrihydrite was synthesized with varying quantities of Pu(IV) following either a sorption or coprecipitation process; the ferrihydrite was then aged hydrothermally to yield goethite. The synthesized materials were characterized via extended x-ray absorption fine structure spectroscopy, transmission electron microscopy, and acid leaching to elucidate the nature of plutonium association with ferrihydrite and goethite. In samples prepared following the sorption method, plutonium was identified in two different forms: a PuO_2 precipitate and a surface sorbed plutonium complex. For the samples prepared via coprecipitation no PuO_2 formation occurs in the ferrihydrite precursor and in the goethite experiments where plutonium concentration is ≤ 1000 ppm (mg Kg^{-1}). In these coprecipitation products plutonium is strongly bound to the minerals either via formation of an inner sphere complex, or via an incorporation process. In the coprecipitation experiments, PuO_2 formation only occurs at the highest plutonium concentration (3000 ppm), suggesting that during ferrihydrite transformation to goethite part of the plutonium can be remobilized to form PuO_2 nanoparticles. Collectively, our results demonstrate that the nature of plutonium associated with the precursor ferrihydrite (adsorbed versus coprecipitated) will have a direct impact on the association of plutonium with its alteration product (goethite). Furthermore, the data illustrate that some properties of plutonium association with the precursor ferrihydrite are retained through the

transformation to goethite. These findings show that plutonium strongly associates to iron (oxy)hydroxides formed through coprecipitation processes and in these materials plutonium can be strongly retained by the iron minerals.

Introduction

The production and testing of nuclear weapons, nuclear accidents, and authorized discharges of radioactive effluents have contributed significantly to plutonium (Pu) contamination in the natural environment. Pu is also a major constituent in civil and military nuclear wastes and is considered a risk-driving radionuclide in the long-term safety of nuclear waste repositories. Due to its long half-life (^{239}Pu $t_{½}$ = 24,100 years) and radiotoxicity, understanding the mobility of Pu in the environment is a key scientific and societal concern.

Several factors can influence Pu mobility in the environment including: Pu redox processes, [1-3] solubility effects, [4, 5] interactions with natural organic matter (including bacteria), [6, 7] and sorption/desorption reactions with mineral surfaces. [8-10] Under typical environmental conditions Pu may exist in the III, IV, V and/or VI oxidation states, each of which demonstrate dramatically different chemical properties. [11, 12]

For example, under environmental conditions the higher oxidation states, V and VI, exist as the highly soluble and mobile PuO_{2}^{x+} moieties. Although Pu(V) and Pu(VI) predominate under oxic conditions, Pu(IV) is often the most common plutonium ion at neutral pH and mildly reducing conditions. [13] Pu(IV) undergoes rapid hydrolysis in circumneutral environments resulting in a significantly lower solubility than the higher oxidations states, V and VI. Pu hydrolysis reactions may occur at Pu(IV) concentrations > 10^{-8} M [14] and result in the formation of discrete $[Pu(OH)_n]^{(4-n)+}$ intrinsic colloids. [5, 13, 15-19] At pH >3 the Pu aqueous concentration is dominated by Pu(V) and by the solubility product of Pu(IV) hydrous oxide precipitate. Although Pu(IV) and

Pu(V) are the most common oxidation states under circumneutral pH conditions, and both sorb to Pu mineral surfaces, Pu(V) has been shown to reduce to Pu(IV) on surfaces. [2, 8, 11, 20-23] Moreover, Pu(IV) has a particularly high affinity for iron (oxy)hydroxides mineral surfaces. [2, 24, 25] Iron (oxy)hydroxides are a common constituent of soils, and predominantly form as an alteration products of iron-bearing minerals. [26] In the deep subsurface iron (oxy)hydroxides may form due to biological oxidation of Fe(II) under reducing conditions. [27] Fe minerals in transient and dynamic (bio)geochemical settings such as sediment deposition in lakes or ponds [28-30], will likely be subject to dissolution and phase transformation reactions [2, 24, 31, 32], and the fate of sorbed species during these processes is currently unknown. In nuclear repositories planned by several countries the first technical containment barrier planned for use consist of stainless-steel canisters. [33-35] Under nuclear repositories conditions the steel cask is expected to corrode over the geological timescales considered [33-35] and depending on the engineered backfill material, the natural bedrock, and the nature of surrounding groundwater, a range of Fe minerals may form during the corrosion process. [36, 37]

Ferrihydrite ($Fe_{9.74}O_{14}(OH)_2$) [38] is a poorly crystalline and metastable early product of both biotic and abiotic precipitation of iron, and is a precursor to more crystalline iron oxide phases such as hematite (α-Fe_2O_3) and goethite (α-FeOOH). Ferrihydrite transformation to either hematite or goethite has been well studied and is strongly dependent upon solution conditions, including pH, ionic strength, and temperature. [39-44] Ferrihydrite typically exhibits a high surface area with a high capacity to adsorb dissolved metal species [45-47], including U, Np, and Pu. [26, 48-51] These traits of ferrihydrite have been utilized to decontaminate radioactive effluent [52] and in various nuclear abatement technologies. [53]

When Pu is present in solutions where iron (oxy)hydroxide minerals may be forming, such as in contaminated ponds, lakes, or streams, or during corrosion of steel, its fate is unknown. The Pu could conceivably adsorb to the newly formed iron oxides (e.g. hematite or goethite), be structurally incorporated into the new phases, or be excluded from the newly formed crystal structure due to crystal-chemical constraints. These three different scenarios have vastly different implications for predicting contaminant transport. Smith et al. [48] demonstrated that under high pH conditions (pH 9), Pu forms an inner-sphere tetradentate complex on the ferrihydrite surface [48] which remains unchanged during transformation to hematite, suggesting that Pu remains strongly adsorbed to the iron (oxy)hydroxide surface [48] during hematite crystallization. Recent experiments by Marshall et al. (2014) [26] and Bots et al. (2016) [49] showed that U(VI) and Np(V) initially adsorbed to ferrihydrite can be incorporated into a distorted Fe(III) octahedral site in the hematite structure during phase transformation. [26,49] The transformation of ferrihydrite to nanoparticulate iron (oxy)hydroxide minerals in the presence of U(VI) resulted in the preferential incorporation of U into goethite (α-FeOOH) over lepidocrocite (γ-FeOOH). [54] At high Pu concentrations (> 10^{-8} M) Pu(IV) intrinsic colloids have been shown to form on the surface of various oxide minerals including iron oxy(hydroxide) minerals. [15, 24, 55, 56] On the goethite surface Pu(IV) colloids may undergo a lattice distortion, due to epitaxial growth, which leads to a stronger surface binding compared to other mineral phases, such as quartz. [15] Both the sorption/desorption of Pu to mineral colloid surfaces (pseudocolloids) and formation of Pu oxide colloids (intrinsic colloids) associated with mineral surfaces, as well as Pu coprecipitation with secondary minerals are all likely important environmental processes under a range of geochemical conditions.[11, 14, 22, 57, 58] For example in groundwater at the Mayak site (Russia) colloidal amorphous iron oxides with associated Pu were found up to 4 km away from the contamination source. [59] In contaminated soils

at Los Alamos National Laboratory, Batuk et al.[60] identified unusual Pu-Fe particles. The authors suggest that the formation of these particles could have resulted from transitory local chemical conditions from the original waste stream. [60] Finally, Lukashenko et al. (2020) [61] identified particles of Pu containing Fe-Mn oxides in bottom sediments of streams flowing from the tunnels in the Degelen Mountain, a site of the USSR nuclear weapon testing program. [61] Analysis of the particles indicate that these materials may be formed as secondary minerals, suggesting that their formation is most likely related to sorption and coprecipitation of transuranic elements with oxides and hydroxides of iron and manganese. [61]

The fate of radionuclides, including Pu, during mineral formation and crystallization processes is still not fully understood. Gaining a detailed, mechanistic, understanding of the interactions between iron (oxy)hydroxides and Pu is key to predicting the long-term stability and mobility of Pu in the natural and engineered environment. The goal of this work is to assess the fate of Pu during the ubiquitous process of ferrihydrite to goethite transformation. We synthesized ferrihydrite with various amounts of Pu(IV) following either a coprecipitation or sorption process, and then subsequently used this material to crystallize goethite. We provide a detailed extended x-ray absorption fine structure spectroscopy (EXAFS) and transmission electron microscopy (TEM) characterization of the synthesized minerals and show that the nature of Pu associated with the precursor ferrihydrite (adsorbed versus coprecipitated) will impact the association of Pu with the ferrihydrite alteration product (goethite).

Methods

Preparation of Pu stock

A ^{242}Pu stock (99.8% ^{242}Pu, 0.12% ^{240}Pu, 0.005% ^{239}Pu, 0.005% ^{238}Pu by activity) was purified using an anion exchange resin (BioRad AG1-X8, 100–200 mesh). Prior to loading on the resin, Pu

was reacted with $NaNO_2$ to convert Pu to Pu(IV). Pu was loaded onto the column in 8 mol/L HNO_3 and the column was subsequently washed with three column volumes of 8 mol/L HNO_3. Pu was stripped from the column using 1 mol/L HCl. The oxidation state of the Pu was determined using the lanthanum fluoride precipitation method [62] and determined to be 97% Pu(III/IV). UV-VIS confirmed that the Pu stock solution was > 95% Pu(IV). The concentration of the purified stock solution was determined by liquid scintillation counting (LSC; Packard Tri-Carb TR2900 LSA) with final concentration of $1.3 \pm 0.1 \times 10^{-3}$ mol/L.

Mineral synthesis

Ferrihydrite *sorption method*: Ferrihydrite (FH) precipitation was induced by drop wise addition of 1-5 mol/L KOH into a 25 mL 0.04 mol/L $FeNO_3.9H_2O$ solution in 30 mL Savillex® PFA (perfluoroalkoxy alkane) vials to yield a final pH ~8. Desired aliquots of a Pu(IV) stock solution were added to the mineral slurries. After addition of the Pu(IV) stock, the pH of the slurries was checked and re-adjusted to the desired value using 1-5 mol/L KOH. The FH-Pu(IV) suspensions were equilibrated for 2 hours. Samples prepared following this sorption method with 3000, 1000, and 400 ppm Pu(IV) will be referred to as FHs-3000, FHs-1000, and FHs-400 respectively.

Ferrihydrite *coprecipitation method*: A 25 mL 0.04 mol/L $FeNO_3.9H_2O$ solution was mixed with desired concentrations of Pu(IV). The solutions were equilibrated for two hours in 30 mL Savillex® PFA vials. Ferrihydrite precipitation was induced by drop wise addition of 1-5 mol/L KOH to a final pH of ~8 and samples with 3000, 1000, and 400 ppm Pu(IV) will be referred to as FHc-3000, FHc-1000, and FHc-400 respectively.

Ferrihydrite transformation to goethite: Goethite (G) was synthesized from hydrothermal alteration of poorly crystalline ferrihydrite (FH) precursors described above, following a modified procedure from Schwertman (2000). [41] The ferrihydrite slurries (FHc-3000, FHc-1000, FHc-400,

FHs-3000, FHs-1000, FHs-400) were adjusted to a pH of 10-11 using 1-5 mol/L KOH. The samples were placed in capped 30 mL Savillex® PFA vials under atmospheric conditions and aged at 80º C for 72 hours in an oil bath to induce ferrihydrite transformation to goethite. The goethite samples will be referred to as G-FHc-3000, G-FHc-1000, G-FHc-400, G-FHs-3000, G-FHs-1000, and G-FHs-400. A schematic of the synthesis routes is presented in Figure 1.

After ferrihydrite and goethite synthesis, the supernatant was allowed to settle for 48 hours, and after sedimentation an aliquot was centrifuged (4000 RCF, 50 minutes, ~ 50 nm particle size cut off) and analyzed for Pu content via LSC. In preparation for the various microscopy and spectroscopy performed on the solid phase, the solids were rinsed and centrifuged (4000 RCF, 50 minutes, ~ 50 nm particle size cut off) three times in Milli-Q water (18.2 MΩ·cm H_2O), to remove soluble salts. After each rinse the supernatant was analyzed for Pu via LSC. Neither sedimentation nor centrifugation is expected to quantitatively remove Pu colloids from solution, since an individual nanoparticle can be as small as 1.5-3 nm and nano particle aggregates may be tens of nm in size. To determine the nature of Pu in the supernatant selected rinse solutions were filtered with 3 kDa ultrafiltration devices (Nanosep 3k Omega; approximate metric size discrimination: 1-2 nm; first rinse of G-FHc-3000, and G-FHs-3000). Results demonstrate that ~80 % of the total Pu in the supernatant is retained by the filter. This fraction of Pu could possibly include Pu associated with fine grained iron oxide minerals and/or Pu nanoparticles aggregates [55], whereas the filtered fraction may include monomeric Pu(IV) [5] and possibly some individual Pu nanoparticles. The synthesis method described here contrasts with the work of Powell et al. [15] and Zavarin et al. [55] who added Pu directly to goethite in batch sorption experiments to examine adsorption and surface precipitation of Pu on the surface of goethite. By comparing these two synthesis strategies, we can gain insights into the mechanisms driving Pu associating with goethite.

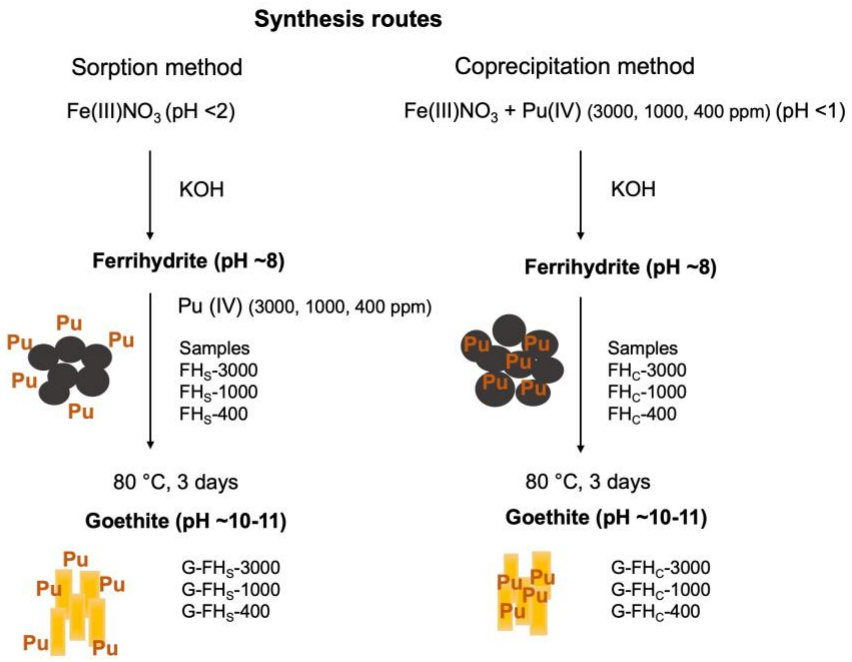

Figure 1: Schematics of synthesis routes of ferrihydrite and goethite solids synthesized via sorption and coprecipitation method. Brown circles represent ferrihydrite precipitates and yellow rectangles represent goethite crystals.

Powder x-ray diffraction

All Pu doped goethite samples were prepared for powder x-ray diffraction (P-XRD) using a Bruker-D8 diffractometer from (5-70º 2θ). 8-10 mg samples were loaded on a domed zero background slide. The domed sample holder is necessary to avoid dispersion of radioactive materials; however, it introduces a high background especially at low angles. The introduction of this background makes it difficult to identify the presence of poorly crystalline-amorphous material in the samples. For both ferrihydrite and goethite, Pu-free samples (FH-blank, G-blank) were prepared following the methodology described above, with which P-XRD measurements could be performed without the use of a domed sample holder.

Oxalate extraction

To quantify ferrihydrite transformation to goethite, an oxalate extraction method was used. [41] For the oxalate extraction, 1 mL of a pH 3 0.2 mol/L ammonium oxalate and 0.2 mol/L oxalic acid solution was added to a 2 mL (1 g/L) mineral slurry aliquot. The samples (G-FHs-3000, G-FHs-1000, G-FHc-3000, and G-FHc-1000) were then reacted in the absence of light on a shaker table for 2 hours to dissolve any non-crystalline component. After 2 hours the samples were centrifuged (5 minutes, 4000 RFC) and the Fe concentration in the supernatant was determined via inductively coupled plasma mass spectrometry (Thermo Fisher Scientific ICAP-Q quadrupole ICP-MS). The oxalate extraction was also performed on one of ferrihydrite sample (FHs-3000).

Transmission electron microscopy

Mineral samples were suspended in ethanol (ferrihydrite) or Milli-Q water (18.2 MΩ·cm) (goethite), sonicated for 5 minutes and added drop-wise onto a copper-supported lacy carbon grid. The samples were imaged using a Titan (FEI) microscope. Imaging was conducted at 300 kV using scanning electron and z-contrast modes. Energy dispersive spectroscopy analyses were performed for selected areas and spots using a FEI SuperX G2 with quad silicon drift detectors. The structure of Pu colloids was investigated using high-resolution transmission electron microscopy (HR-TEM) and scanning transmission electron microscopy (STEM).

Pu acid extraction

Sequential acid extraction was performed to determine the leachability of Pu from the Pu doped goethite samples (G-FHs-3000, G-FHs-1000, G-FHc-3000, and G-FHc-1000). Mineral suspensions (0.33 g / 100 mL) were equilibrated in increasingly higher molarity HNO_3 solutions (0.001-4 M) for 30 minutes. After 30 minutes extractions, the mineral-acid suspensions were centrifuged (10 minutes, 8500 RCF, size discrimination 100 nm) and the supernatant was analyzed to determine the Pu concentration via LSC. For G-FHc-3000, G-FHs-3000 an aliquot of the

leached solution was filtered using a 3 kDa ultrafiltration device (Nanosep 3K Omega; approximate metric size discrimination: 1-2 nm). For both G-FHc-3000 and G-FHs-3000 the mineral suspensions in 4 M HNO_3 were reacted for an additional 20 hours. Samples were then centrifuged (10 minutes, 8500 RCF) and the Pu concentrations in the supernatant were measured. A parallel experiment was performed on Pu-free goethite to determine the leachability of Fe. Fe concentrations in leached solutions were determined via ICP-MS (Thermo Fisher Scientific ICAP-Q quadrupole ICP-MS).

Extended x-ray absorption fine structure spectroscopy

Selected ferrihydrite and goethite mineral phases were isolated from the experiments via centrifugation (5 minutes, 4000 RCF), mixed with glycerol, and mounted into custom made indium sealed, triple contained, aluminum sample holders. All extended x-ray absorption fine structure spectroscopy (EXAFS) data were collected on beamline 11-2 at the Stanford Synchrotron Radiation Lightsource, Stanford CA. Pu L_{III}-edge (18057 eV) EXAFS data were collected in fluorescence mode using a 100 element Canberra Ge detector (corrected for dead time) with a Si(220) (ϕ=0°) double monochromator detuned to 50% intensity. All samples were held in a LHe cryostat at 30 K throughout analysis. Data reduction and analysis were conducted using the RSXAP software suite [63, 64, 65] in conjunction with backscattering lineshapes and phases calculated using FEFF8.5L. [66] The EXAFS data were fitted in R-space. Error analysis was performed using a profiling method. [67] In all cases the total number of fitting parameters was less than two-third of the total number of independent points.

Results and discussion

Ferrihydrite and goethite synthesis in the presence of Pu(IV) After ferrihydrite and goethite were synthesized, the minerals were characterized by P-XRD, TEM, and oxalate extraction.

P-XRD of all goethite samples (G-FHs-3000, G-FHs-1000, G-FHs-400, G-FHc-3000, G-FHc-1000, G-FHc-400) and of a Pu-free goethite sample were collected, and additional peaks beyond those characteristic of goethite were not identified (Figure 2). The P-XRD pattern of ferrihydrite was collected for FH-blank, a Pu free sample, and the broad peaks at 34° and 65º of 2θ are characteristic of two-line ferrihydrite. [41] TEM photomicrographs of the solid samples illustrate the crystal morphology of nanocrystalline FHc-3000, and G-FHc-3000 (Figure SI 1). The ferrihydrite nanoparticles are poorly crystalline and range in size between 3-5 nm, whereas the acicular goethite grains are crystalline and are 1-3 μm long and 10-100 nm wide. These crystal morphologies are consistent with ferrihydrite and goethite materials. [41] Oxalate extraction of G-FHs-3000, G-FHs-1000, G-FHc-3000, and G-FHc-1000 confirmed that > 99 % of ferrihydrite recrystallized to more ordered forms. As expected, the oxalate extraction of FHs-3000 showed a total recovery of Fe (99.99%). The P-XRD, TEM analysis, and oxalate extraction results indicate that the addition of Pu does not affect the nature of the synthesized products (Figure 2).

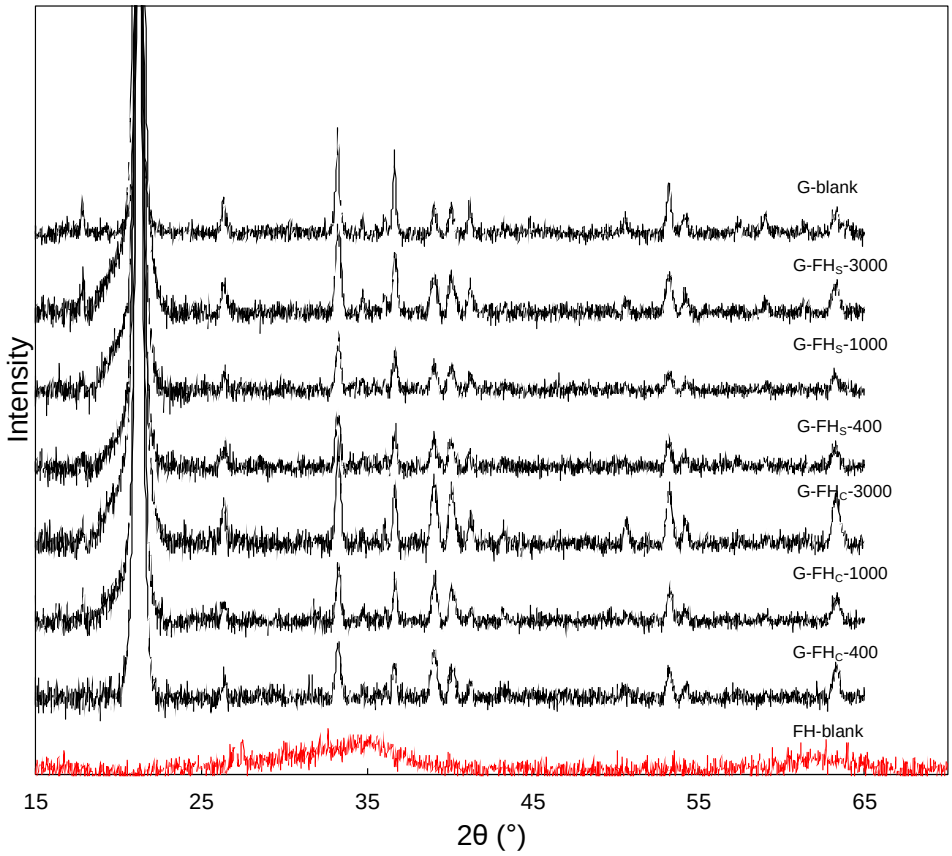

Figure 2: P-XRD pattern of Pu-free ferrihydrite and goethite (FH-blank, G-blank) and goethite samples G-FHc-3000, G-FHc-1000, G-FHc-400, G-FHs-3000, G-FHs-1000, and G-FHs-400.

The analysis of the supernatant from all ferrihydrite syntheses indicated that 99.9% of Pu had been removed from solution upon reaching the desired pH of ~8. After ferrihydrite hydrothermal transformation to goethite, the concentration of Pu in the supernatant was monitored again and results show that for all samples < 0.8 % Pu was released in solution during rinsing (Figure SI 2). The results indicate that a strong association between Pu and the iron (oxy)hydroxide solids is preserved during ferrihydrite transformation to goethite, although a fraction of Pu may be mobilized during this process.

The HR-TEM imaging and elemental mapping of G-FHs-3000 and G-FHs-1000 revealed the presence Pu nanoparticles. As calculated from several TEM images, the size of the nanoparticles ranges from 3 to 5 nm, which is consistent with the 2.5-5 nm size range for PuO_2 reported in the literature. [5, 16-18, 55] Electron diffraction analysis of the HR-TEM data confirm that the observed nanoparticles have the expected *fcc* PuO_2 structure with Fm3m space group (d1 (Å) 3.08(1) and d2 (Å) 2.61(2)) [15] (Figure 3). The observed PuO_2 structure is in contrast to the structure of Pu_4O_7 nanoparticles observed by Powell et al. (2011) [15] and Zavarin et al. (2014) [55] using TEM. The experiments of Zavarin et al. (2014) [55] examined the structure of Pu nanoparticles formed on the surface of goethite by the addition of a Pu source (either in the form of aqueous Pu(IV) or PuO_2 nanoparticles) in batch sorption experiments at 25°C and 80°C for over 100 days. Their results showed that once formed, the Pu_4O_7 nanoparticles were stable at 80°C for over 100 days; however, when PuO_2 nanoparticles were added as a source of Pu, they did not alter to Pu_4O_7. The formation of distorted Pu_4O_7 nanoparticles with *bcc* structure is interpreted as a result of a strong binding of Pu with the goethite surface leading to epitaxial growth. [15, 55] Given that we did not observe the formation of Pu_4O_7 nanoparticles via HR-TEM imaging, we must conclude that our synthesis pathways were not dominated by the epitaxial growth of Pu nanoparticles on the goethite surface. Instead, it is likely that PuO_2 observed here was formed during the ferrihydrite precipitation step, or in solution during ferrihydrite alteration to goethite, thus suggesting that the synthesis pathway affects the final state of Pu on the goethite surface. Nevertheless, the presence of Pu nanoparticulate in these samples is not unexpected. In the synthesis of the samples synthesized following the sorption method, a Pu stock is added to a ferrihydrite slurry solution at pH ~ 8, and starting at circumneutral pH values and at the Pu concentrations used in these experiments ($> 10^{-8}$ M), Pu(IV) is generally expected to undergo rapid hydrolysis to form PuO_2 solids. [5, 12]

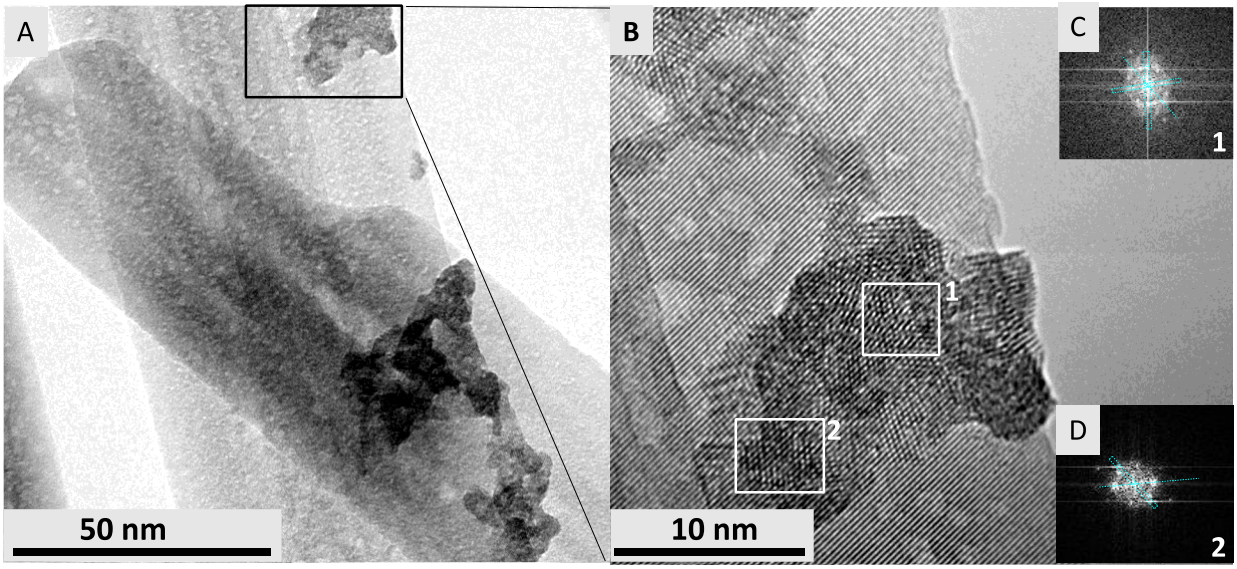

Figure 3: Pu nanoparticles on goethite G-FHs-3000. (A) Low-magnification TEM image of large tabular goethite and intrinsic Pu nanoparticles (black inlet). (B) HR-TEM image of Pu nanoparticles on goethite surface from inlet in (A); (C) and (D) Fast Fourier Transform (FFT) of HR-TEM area 1 and 2 shown in panel (B), is consistent with the *fcc*, PuO_2 structure.

HR-TEM imaging revealed the presence of PuO_2 precipitates (*fcc*, d1 (Å) 3.08(2) and d2 (Å) 2.61(2)) in the high Pu concentration G-FHc-3000 (Figure 4) however, PuO_2 nanoparticles were not identified in G-FHc-1000 and G-FHc-400. Furthermore in G-FHc-1000 and G-FHc-400 the Pu concentration was too low to be detected using STEM-TEM indicating that Pu is either dispersed on the surface of goethite and/or incorporated into the solid phase.

Unfortunately, the ferrihydrite nanoparticles are 3-5 nm in size, which is similar to the expected PuO_2 nanoparticles size observed in the goethite samples (3-5 nm). This similarity in size between Pu nanoparticles and the ferrihydrite substrate creates difficulties in the identification and distinction of PuO_2 via TEM imaging (i.e. the needle in a haystack problem). For this reason, TEM

was not sufficient to identify whether Pu nanoparticles were present in the ferrihydrite samples (FHs-3000 and FHc-3000), and we turn to EXAFS as a more definitive confirmation (below).

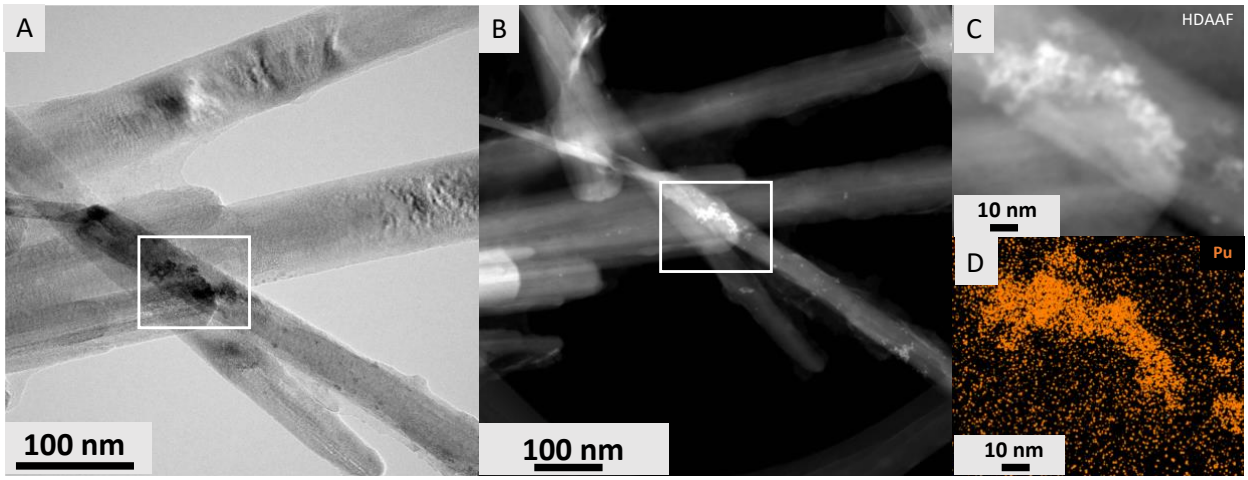

Figure 4: PuO_2 nanoparticles on goethite G-FHc-3000. (A) Low-magnification TEM and (B) STEM image of large tabular goethite and PuO_2 (white inlet). C) STEM and D) Pu elemental map of Pu nanoparticles.

Reversibility of Pu associated with ferrihydrite and goethite In an effort to understand the reversibility of Pu associated with the goethite, acid leaching experiments were performed. In 4-hour sequential leaching experiments (0.001-4 M) a total of 9.6 ± 0.2% and 3.42 ± 0.3% of Pu is leached from G-FHs-3000 and G-FHs-1000, respectively, whereas 4.03(12)% and 1.54(8)% of Pu is leached into solution from G-FHc-3000 and G-FHc-1000, respectively (Figure 5). The centrifuged supernatant likely includes particles < 100 nm (Pu associated with goethite and/or Pu nanoparticles aggregates), and Pu aqueous species in the form of aqueous Pu(IV) at lower pH

values. 5 Upon filtration with a 3 kDa filter of GFHs-3000 and G-FHc-3000 up to 70% of the total Pu is retained by the filter, however as expected by thermodynamic and solubility considerations 5 the amount of Pu filtered through a 3 kDa filter increases as the acidity of the leaching solution increases (Figure SI 3). After an additional 20 hours of leaching in a 4 mol/L HNO_3 solution, a total of 40(1)% of Pu is leached from G-FHs-3000, whereas only 7.5(5)% of total Pu is leached from G-FHc-3000 (Figure 5). In the Pu-free goethite leaching test, $< 0.05 \pm 0.003$ % Fe was dissolved after 24 hours, indicating that goethite dissolution during the leaching process was minimal (Figure SI 4).

Overall the majority of Pu remains associated with goethite, and in all experiments < 40% of Pu is leached from goethite, regardless of the synthetic route. Differences in synthetic pathways, however, appear to have an impact on the nature of Pu association with the hydrothermally transformed product (goethite), as in just 4 hours of sequential leaching (Figure 5) 2-3 times more Pu is leached from goethite recrystallized following the sorption process, compared to the coprecipitated samples. These results suggest that Pu associated to ferrihydrite/goethite through the sorption method may be more labile than Pu coprecipitated with ferrihydrite/goethite. Furthermore the fact that a larger fraction of Pu is leachable in high Pu concentration compared to low Pu concentration samples suggests that the fraction of surface associated Pu increases with concentration. This increase may indirectly suggest a limited capacity for Pu to be incorporated into the goethite phase (and not susceptible to leaching). Leaching experiments could not be performed on the ferrihydrite samples due to the enhanced dissolution of ferrihydrite in the chosen experimental conditions, nonetheless these results, suggest that some properties of Pu association with the precursor mineral are retained through the transformation of ferrihydrite to goethite.

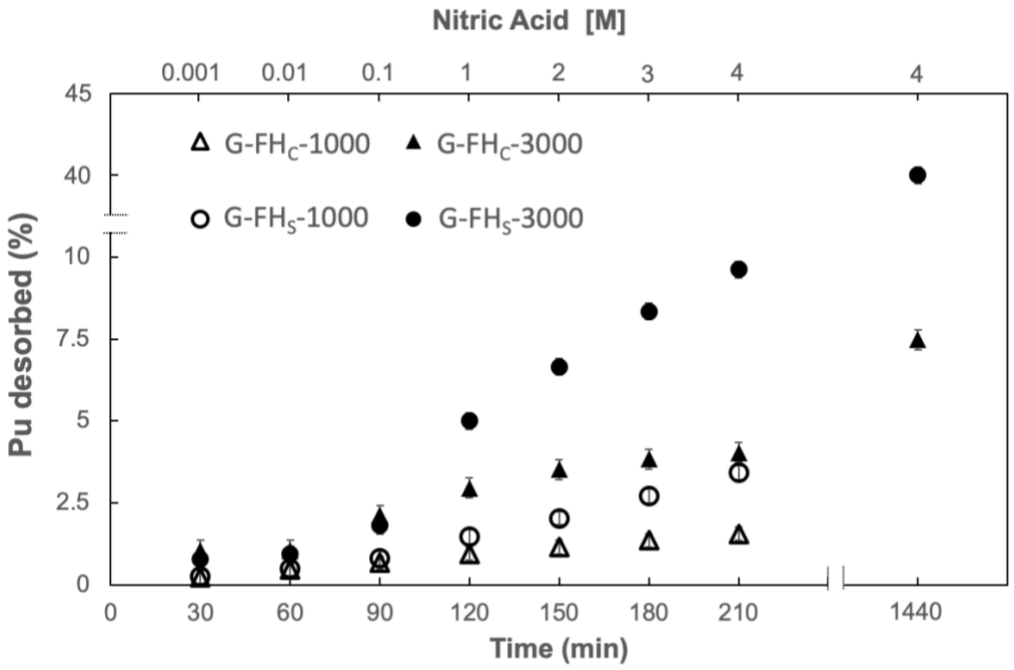

Figure 5: Leaching behavior of Pu in acidic solutions (0.001-4 M) for goethite synthesized following the sorption (G-FHs-3000, G-FHs-1000) and coprecipitation (G-FHc-3000, G-FHc-1000) method. Data shown with 2σ errors.

The structure of Pu associated with ferrihydrite and goethite using EXAFS A representative set of ferrihydrite and goethite samples were analyzed using EXAFS spectroscopy in order to characterize the nature of Pu binding with these mineral phases. Three samples following the sorption method, FHs-3000, G-FHs-3000, and G-FHs-1000 were analyzed in addition to four samples that were produced from the coprecipitated method, FHc-3000, G-FHc-3000, G-FHc-1000, and G-FHc-400. The background-subtracted Pu L_{III}-edge EXAFS spectra and the corresponding Fourier transforms (FT) for ferrihydrite and goethite systems are shown in Figure 6 and Figure 7, and fitting results for all datasets are detailed in Table 1. Corresponding x-ray

absorption near edge spectra for these samples are shown in Figure SI 5 and calculated edge inflection energies tabulated in Table SI 1.

Ferrihydrite The EXAFS spectrum of FHs-3000 was successfully modeled with a single Pu-O shell consisting of 9(1) scatterers (i.e. coordination number) at 2.31(1) Å. A further two peaks were evident in the FT at r > 2.5 Å. Note that we refer to the x-axis of the FT as r, which differs from pair distances (R) due to known shift effects. [66] The first of the two peaks was successfully modeled as 6(4) Pu-Fe scatterers at 3.39(1) Å with an elevated Debye Waller factor (σ_2; pair-distance distribution variance) of 0.021(4) $Å_2$, which implies a broad distribution of Pu-Fe distances. Alternatively, as σ_2 and coordination number are correlated in the EXAFS equation it could be that the number of Pu-Fe scatterers is being overestimated. Normally, this correlation would be accounted for in the error estimates; however, in the case of non-Gaussian pair-distance distributions (e.g. a split-shell that is not resolved), the error estimates and best-fit parameters can be inaccurate. For example, Table SI 2 shows two alternative fitting models for this dataset. The first demonstrates that fixing the number of coordinating Fe atoms to 3 still produces a high-quality fit while reducing the σ_2 to a more reasonable (albeit still elevated) 0.015 $Å_2$. The second fit utilizes a Pu-Fe shell that was allowed to split into two. This model produced a fit with 1.9(5) and 1.0(5) Pu-Fe scatterers at 3.28(5) and 3.43(3) Å, respectively. Given these alternative fits it seems likely the number of Pu-Fe scatterers is being significantly overestimated in our standard fit and the true value is more in line with a Pu-ferrihydrite sorption complex. The second peak was modeled with 3(1) Pu-Pu scatterers at 3.79(1) Å, consistent with expectations for PuO_2 (3.82 Å). [68] Given the identification of both Pu and Fe scatterers in the EXAFS it is very likely that in FHs-3000 Pu(IV) is present in two distinct coordination environments: PuO_2, and an additional adsorbed, poorly defined, inner-sphere complex on the ferrihydrite surface. Recent reports of various actinides

(An=Th, U, Np, Pu) adsorbed onto Fe containing minerals show An-Fe distances varying from 3.35-3.7 Å [48, 69-73], consistent with our modeled 3.39(1) Å Pu-Fe distance. Alternatively, these EXAFS data could be explained by a coordination environment containing an interaction between PuO_2 and the ferrihydrite surfaces i.e. a PuO_2 nanoparticle associated with the ferrihydrite where it can 'see' surface Fe atoms. This could also explain some of the high Debye-Waller factors we observe. However, on balance, a dual coordination environment with PuO_2 and a Pu-ferrihydrite complex seems more likely, especially given the similarity in reported Pu-Fe distances. It is difficult to quantify the relative proportions of these two Pu species (inner-sphere and PuO_2) as EXAFS analysis only provides an average coordination environment around the Pu atom. However, we can use our knowledge of the PuO_2 structure to put a lower limit on the amount of PuO_2 in the sample. The structure of bulk PuO_2 consists of 12 Pu atoms at 3.82 Å [68], which given our fitted coordination number of 3 Pu atoms would imply the minimum proportion of PuO_2 in this sample is ~25%. However, the number of Pu atoms reduces as PuO_2 moves away from a bulk material into a nanoparticulate form due to Pu atoms near the surface having fewer Pu neighbors (Figure SI 6). [70, 74] This effect is well demonstrated for PuO_2 nanoparticles by recently Micheau et. al., 2020 [18], which demonstrated that EXAFS can significantly underestimate particle size when comparing to small angle x-ray scattering measurements. Therefore, due to these effects, this value only represents a *lower limit* on the proportion of PuO_2 in the sample. This also implies the maximum proportion of PuO_2 that is surface adsorbed is 75%. Overall, the EXAFS results indicate a significant degree of surface adsorption and PuO_2 precipitation.

The EXAFS spectrum of Pu associated with FHC-3000 was successfully modeled with a split O environment, including 3.0(1) and 4.0(2) Pu-O scatterers at 2.24(1) and 2.41(1) Å, respectively. In contrast to FHS-3000, only one additional peak was evident in the FT which was successfully fit

with a single Pu-Fe shell at 3.39(1) Å. Interestingly this shell was fit with a high number (8 ± 1) of Pu-Fe scatterers albeit with a very high σ^2 of 0.026(3) Å^2. The high uncertainties associated with this fit make the exact nature of the Pu-ferrihydrite complex difficult to elucidate, but it could represent a replacement of the Fe^{3+} ion with a Pu^{4+} in the ferrihydrite solid. The large discrepancy in the size of Fe^{3+} and Pu^{4+} ions (0.645 and 0.96, respectively [75]) make this substitution unlikely without significant disruption to the local structure. However, our EXAFS data do indicate highly elevated σ^2 values suggesting a broad range of Pu-Fe pair distances, and lack long-range order that would be evidenced by multiple Pu-Fe shells. The local environment around Fe in the ferrihydrite structure consists of Fe atoms at ~3.04 and 3.44 Å, although due to the poorly crystalline nature of ferrihydrite, its structure has still not been fully resolved. [38, 76] Although highly disordered a Pu-Fe distance of 3.39(1) Å could correspond to corner sharing between metal polyhedral in the ferrihydrite structure. [76, 77]

The σ^2 and coordination number parameters in the EXAFS equation are commonly correlated in the fit results; [78] therefore, the elevated σ^2 values fitted here suggest either a large amount of structural disorder (i.e. a broad distribution of Pu-Fe pair distances) or that the number of Pu-Fe scatterers is being overestimated. For example, constraining the number of Pu-Fe scatterers to 4 reduced σ^2 to 0.013(2) Å^2 while still maintaining a reasonable fit albeit with an increased fit residual factor (*R* %) (7.9 vs 3.5 %); thus, it cannot be excluded that the EXAFS data may represent a surface complex with a lower number of Pu-Fe scatterers. [48, 69-73] Interestingly, the EXAFS spectrum and resultant fit for FHC-3000 bears a striking resemblance to what was collected in similar experiments by Smith et al., [48] where ferrihydrite precipitation was induced from a Pu-HNO_3 solution at pH 9. PuO_2 formation was not observed and the data were modeled with 4 Fe scatterers at 3.38(2) Å and attributed to the formation of a polynuclear multidentate complex with

the ferrihydrite surface. In contrast to FHs-3000 no Pu-Pu scatterers could be identified in the FHc-3000 EXAFS spectrum precluding the possibility of PuO_2 formation in this sample and demonstrating that Pu(IV) is associated with the ferrihydrite solid before PuO_2 precipitation could occur. The association of Pu to a Fe(III) precipitate in the materials formed during the coprecipitation method is possible as the coprecipitation synthesis starts from an aqueous solution at pH<1 and according to thermodynamic considerations, in these solution conditions, Fe(III) hydrolysis precipitates may form in solution starting at pH 1-2 (Figure 1). [79, 80]

Goethite the EXAFS spectra of the goethite samples recrystallized from the hydrothermally altered Pu-sorbed ferrihydrite (G-FHs-3000 and G-FHs-1000) are similar and both spectra could be fit using a two-shell model. The first shell in both cases was successfully fit with 8(1) Pu-O scatterers at 2.32(1) Å and the second peak in the FT was fit with 4(1) Pu-Pu scatterers at 3.80(1) Å strongly supporting the formation of PuO_2 solids in these systems. However, the modeled Pu coordination numbers are low compared to expectations for PuO_2 and suggest either PuO_2 is present as very small nanoparticulate < 1 nm (Figure SI 6) or that a second Pu species is present as an adsorbed or coprecipitated inner sphere complex. We use a similar approach with this sample as we used with FHs-3000 and attempt to put a lower limit on the quantity of PuO_2 present. If we assume Pu is present as bulk (as opposed to nanoparticulate or surface adsorbed)-PuO_2 with a Pu-Pu coordination number of 12, the number of Pu-Pu scatterers in both samples being fitted as 4(1) would indicate a minimum of 33% Pu is present as PuO_2 in this system, not unlike the FHs-3000 precursor.

In this case, if the TEM characterized particles are representative of the average, the remaining Pu would have to be present as a surface complex. Unfortunately, while it was possible to include Pu-Fe scatterers in the fit their presence was unable to pass an F-test [81] so we cannot conclusively

demonstrate an inner-sphere surface complex, however, this does not exclude the possibility of a surface complex entirely. For example, Pu may be present as an inner sphere complex with a very broad range of Pu-Fe pair distances making it very difficult to discern using EXAFS analysis. Interestingly, the minimum proportion of PuO_2 in the sample remains the same, prior to and after ferrihydrite transformation to goethite. This, in turn, may indicate that the PuO_2 does not undergo any transformation during the alteration of ferrihydrite to goethite.

Overall the EXAFS fits and TEM characterization support PuO_2 formation in G-FHs-3000 and G-FHs-1000. The EXAFS data also suggest that Pu in these samples may be present in dual coordination environment with PuO_2 accounting for a minimum of 33% of Pu, and the remainder being present as poorly defined surface complex since no Pu-Fe scatterers could be conclusively identified in this sample. [11, 12] Though it is important to stress that the PuO_2 calculation represents a floor (i.e. a minimum) and the real value is likely to be much higher due to nanoparticle / surface effects. The high percentage of Pu detected in the acid extraction of G-FHs-3000 and G-FHs-1000, is consistent with the presence of Pu as a surface complex, where the leached fraction could represent any bound Pu being easily leached from the goethite surface. Collectively, these data demonstrate that in the ferrihydrite and goethite samples synthesized following the sorption method a fraction of Pu will be found as intrinsic PuO_2 nanoparticles, and the PuO_2-like coordination environment is preserved during mineral phase transformation. The EXAFS data also demonstrate that Pu adsorbed to ferrihydrite may be remobilized, as evidenced by the changes in coordination environment of the Pu sorbed species from the ferrihydrite precursor (FHs-3000) to the recrystallized products (G-FHs-1000 and G-FHs-3000) (Table 1).

The EXAFS spectrum of the Pu associated with G-FHc-3000 was successfully modeled with 6(1) Pu-O scatterers at 2.28(1) Å and 1 (1) Pu-Fe scatterers at 3.56(1) with σ_2 values of 0.013(2)

and 0.003(1) $Å_2$, respectively. The Pu-Fe σ_2 is very low and probably represents an underestimation of the number of Pu-Fe scatterers due to the coupling between σ_2 and coordination number in the EXAFS equation. Additionally, a peak at 3.7 Å was successfully modeled as 2(1) Pu-Pu scatterers at 3.80(1). The clear identification of Pu-Pu scatterers in the FT demonstrates the presence of PuO_2. Interestingly, no PuO_2 was observed in the ferrihydrite precursor (FHC-3000) indicating that Pu(IV) was probably excluded from the ferrihydrite structure or surface in the ferrihydrite transformation reaction where it subsequently underwent precipitation as PuO_2. As with the other observations of Pu-Pu scatterers in other samples presented here, the low coordination numbers suggest PuO_2 accounts for only a fraction of all Pu in this sample. A pair of Pu-Pu scatters would imply a minimum of 17% PuO_2 in this experiment. The presence of Pu-Fe peaks suggests that the non-PuO_2 fraction of Pu in this sample may be present as an inner sphere complex adsorbed on the surface of goethite. Importantly, the result suggest that high Pu concentrations associated with ferrihydrite may lead to the formation of PuO_2 during the transformation of ferrihydrite to goethite.

The G-FHC-1000 and G-FHC-400 samples displayed similar spectra with three easily identifiable peaks in the FT at r ≈1.5 Å, 2.5 Å, and 3.2 Å. The first peak at 1.5 Å was successfully fit with an Pu-O shell 6(1) scatterers at 2.21(1) Å. Oxygen shells in both G-FHC-1000 and G-FHC-400 have σ_2 factors of 0.013(2) and 0.016(2) $Å_2$ implying a broad distribution of Pu-O pair distances. This reduction in oxygen atoms coordination from 8 in the other systems to 6 here is interesting as the Fe^{3+} is coordinated by 6 oxygen atoms in the goethite structure. Additionally, the Pu-O bond distances of 2.21 Å are significantly shorter than would be expected for a Pu(IV) surface complex and is closer to the Fe-O bond distance in goethite at ~2.1 Å. [82, 83] This bond distance is significantly shorter than the G-FHC-3000 sample which was fitted with a Pu-O distance of 2.28 Å. This

lengthening of the bond with concentration can probably be attributed to an averaging effect caused by the presence of two distinct coordination environments: one with a shorter Pu-O distance like we see here for G-FHc-400 and G-FHc-1000; and second more typical of a PuO_2 environment. The second and third features in the FT were too short to be associated with Pu-Pu scatterers; therefore, they were modeled as two Fe shells. These were fitted as 6(1) Pu-Fe scatterers at 3.17(4) Å and 10(8) Pu-Fe scatterers at 3.49(2) Å with an elevated σ^2 factor of 0.010(1) $Å^2$ for G-FHc-1000. This result is similar to G-FHc-400 where the second and third features in the FT were fit as 5(3) Pu-Fe scatterers at 3.19(1) Å and 8(4) Pu-Fe scatterers at 3.47(2) Å. The high number of Fe atoms and the large estimated errors associated with those parameters in G-FHc-1000 and G-FHc-400 makes it difficult to draw any firm conclusions about the exact nature of the local structure in the Pu-goethite complex. However, collectively, these EXAFS data could indicate that some kind of incorporation into the goethite structure is occurring. Firstly, there is the reduction of in the number of Pu-O scatterers to ~6 and concurrent contraction in the Pu-O bond length to just ~2.2 Å which seems more plausible for the Pu^{4+} ion in a goethite-like structure rather than a surface complex. Furthermore, the local environment around Fe in the goethite structure consists of 2, 2, and 4 Fe neighbors at ~3, ~3.3 and ~3.4 Å, respectively. [82, 83] These distances are not unlike our fitted distances of 3.2 and 3.5 Å and, given the large error bars associated with our fits our data is compatible with Pu^{4+} incorporated into goethite. As was discussed previously the difference in size between Fe^{3+} and Pu^{4+} make direct and stable substitution into the goethite structure unlikely without significant disorder in the local and long-range structure. Interestingly, the σ^2 in our fits suggest elevated levels of local structural disorder around the Pu atom. Other possible explanations for the local Pu structure observed are the formation of a surface complex on the goethite surface; however, the shortest modeled Pu-Fe distance at 3.19(2) Å is significantly shorter than the range

of An-Fe distances previously reported (3.35-3.7 Å). [48, 69-73] Lastly the EXAFS data are not inconsistent with the formation of a distinct poorly ordered Pu-Fe solid phase as has been hinted at in forensics literature, [60] although the formation of a distinct Pu-Fe phase was not supported by TEM imaging. Overall the TEM and EXAFS data demonstrate that PuO_2 exists at the highest concentration Pu coprecipitation samples (3000 ppm) but not the lower concentrations (1000 and 400 ppm). This suggests that during ferrihydrite phase transformation at higher Pu concentration (0.06 mmol/L Pu(IV) in solution, 3000 ppm Pu(IV) in the solid) part of the Pu associated to the ferrihydrite precursor FHC-3000 will be remobilized and form PuO_2 nanoparticles. Furthermore there is evidence that during ferrihydrite transformation at high Pu concentration a fraction of the Pu remains strongly bound to the goethite surface (Table 1). No PuO_2 was observed in the ferrihydrite precursor (FHC-3000) or in the lower concentration goethite samples (G-FHC-1000 and G-FHC-400). The presence of two distinct Pu-Fe shells in G-FHC-1000 and G-FHC-400 (at 3.20 Å and 3.49 Å) compared to the ferrihydrite precursor FHC-3000 (one shell at 3.41 Å) suggest that the Pu binding site changes significantly during iron oxide transformation. Even though Pu coordination changes during phase transformation, these experimental conditions do not favor PuO_2 precipitation. It is difficult to determine the exact nature of Pu in solids prepared following the coprecipitation process; however, the data clearly show that Pu is strongly bound to the minerals either by the formation of a strong inner sphere complex, or via an incorporation process.

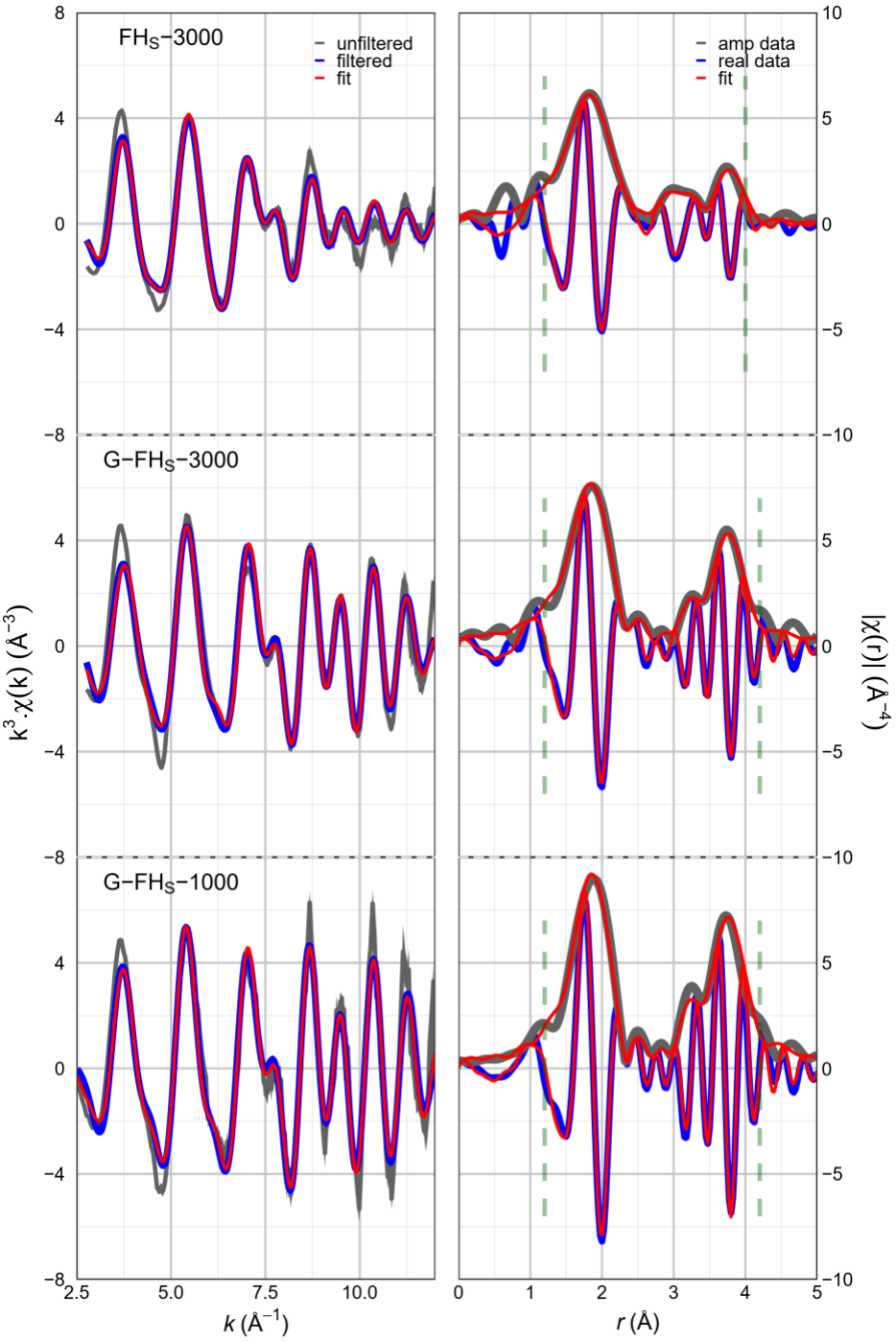

Figure 6: Pu LIII-edge EXAFS data and fit results for samples synthesized following the sorption method measured at 30 K. Left: EXAFS results in k-space. Right: Fourier transforms (FT) of the k-space data and fit. Vertical dashed lines indicate the fit range. Data were transformed between

2.5 and 12 $Å^{-1}$ by using a Gaussian window with a width of 0.3 $Å^{-1}$. The raw unfiltered data error bars (encompassed by the solid gray shaded area around the data set) were estimated by the standard deviation of the mean between traces.

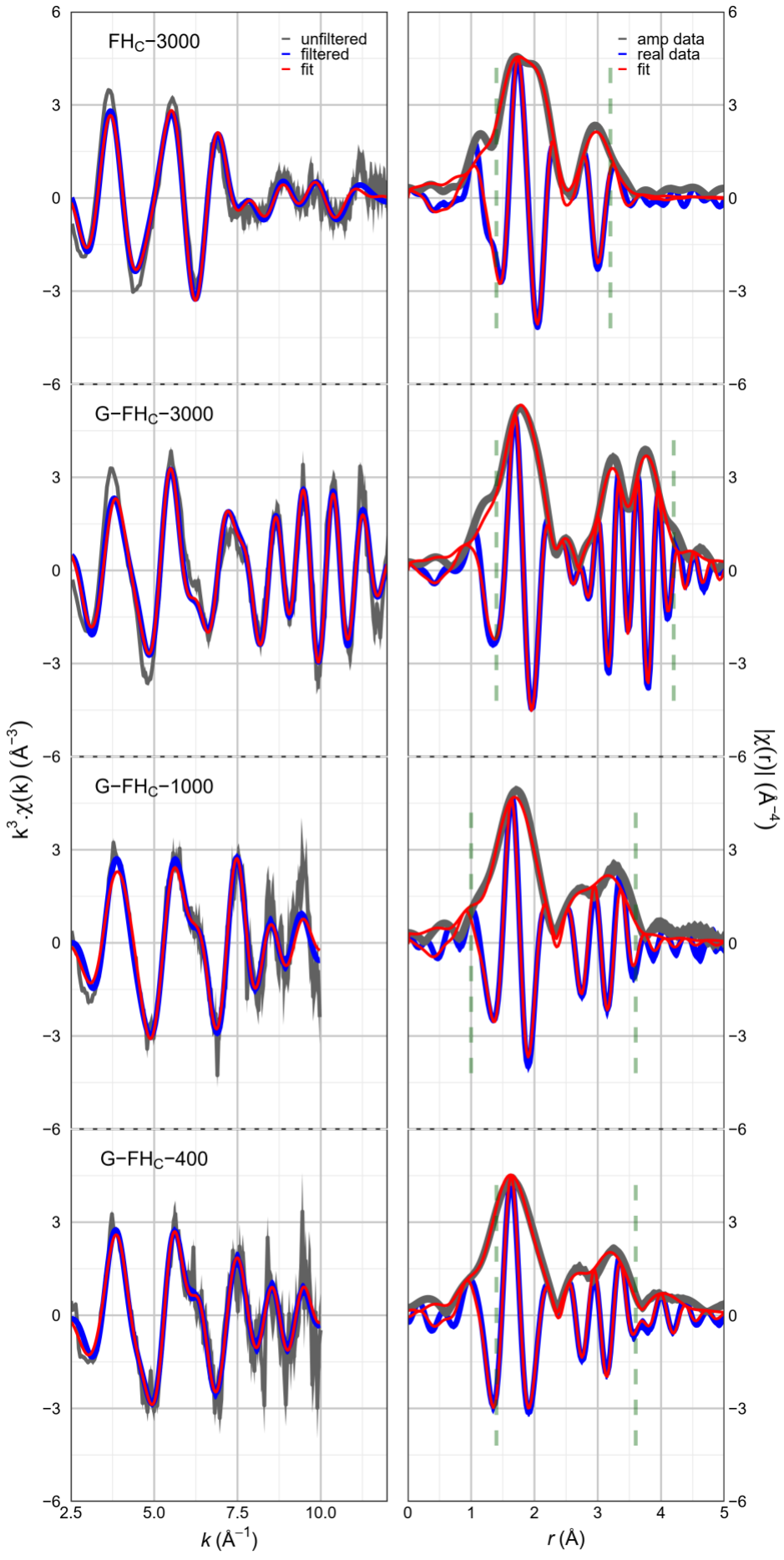
FHC−3000
unfiltered
filtered
fit
amp data
real data
fit
G−FHC−3000
G−FHC−1000
G−FHC−400
k3.χ(k) (Å−3)
|χ(r)| (Å−4)
k (Å−1)
r (Å)
2.5
5.0
7.5
10.0
0
1
2
3
4
5
6
3
0
−3
−6

Figure 7: Pu L_{III}-edge EXAFS data and fit results for samples synthesized following the coprecipitation method measured at 30 K. Left: EXAFS results in k-space. Right: Fourier transforms (FT) of the k-space data and fit. Data are transformed over the displayed range in k-space. Vertical dashed lines indicate the fit range. See Figure 6 for further details.

Table 1: Summary of EXAFS fit results

Sample	Shell	N	R (Å)	σ_2 (Å$_2$)	ΔE_0 (eV)	*R* (%)
FHs-3000	Pu-O	9(1)	2.31(1)	0.014(1)	-10.8(8)	8.0
	Pu-Fe	6(4)	3.39(1)	0.021(4)		
	Pu-Pu	3(1)	3.79(1)	0.008(1)		
FHc-3000	Pu-O1	4.0(2)	2.41(1)	0.005(1)*	-11.0(4)	3.5
	Pu-O2	3.0(1)	2.24(1)			
	Pu-Fe	8(1)	3.39(1)	0.023(2)		
G-FHs-3000	Pu-O	8(1)	2.32(1)	0.010(1)	-11.4(8)	10.2
	Pu-Pu	4(1)	3.80(1)	0.003(1)		
G-FHs-1000	Pu-O	8(1)	2.32(1)	0.008(1)	-11.7(7)	9.9
	Pu-Pu	4(1)	3.81(1)	0.001(1)		
G-FHc-3000	Pu-O	6(1)	2.28(1)	0.013(2)	-12.6(12)	8.7
	Pu-Fe	1(1)	3.56(1)	0.003(4)		
	Pu-Pu	2(1)	3.80(1)	0.001(1)		
G-FHc-1000	Pu-O	5(1)	2.21(1)	0.013(2)	-10.0(16)	13.3
	Pu-Fe	6(1)	3.17(4)	0.01(1)*		
	Pu-Fe	10(8)	3.49(2)			
G-FHc-400	Pu-O	6(1)	2.20(2)	0.016(2)	-7.6(21)	12.2
	Pu-Fe	5(3)	3.19(2)	0.015(6)*		
	Pu-Fe	8(4)	3.47(2)			

*indicates a tied σ_2 parameter (i.e. shared in two shells). N represents the coordination number assuming an amplitude reduction factor of 1; R denotes the interatomic distance; σ_2 represents the Debye Waller factor; ΔE_0 represents the energy shift from the calculated energy Fermi level.

Conclusions

In this study we investigated the fate of Pu during iron oxide crystallization and phase transformation via TEM imaging, EXAFS and chemical analysis. We show that variations in synthetic routes impact the nature of Pu associated with both the ferrihydrite precursor and the ferrihydrite phase-transformed product (goethite). When a Pu containing solution is added to a ferrihydrite mineral (sorption route), a fraction of the Pu precipitates as PuO_2 nanoparticles and the remaining Pu fraction forms a complex on the mineral surface. After hydrothermal alteration to goethite, the PuO_2-like nanoparticle is preserved as demonstrated by TEM imaging, and a fraction of Pu is still present as a surface adsorbed species on the goethite mineral surface. There is evidence that this adsorbed species is more weakly bound to goethite than to ferrihydrite, as demonstrated by a lack of Pu-Fe scatteres in the goethite samples compared to the ferrihydrite precursor. This observation suggests that Pu adsorbed to ferrihydrite may be mobilized during the phase transformation. The analysis of the supernatant after hydrothermal alteration of ferrihydrite to goethite showed a small increase in Pu concentration confirming that some Pu re-mobilization occurs during ferrihydrite transformation to goethite.

When ferrihydrite is precipitated directly from a solution containing Fe and Pu (coprecipitation route) no PuO_2 is observed. Although it is difficult to identify the exact nature of Pu in the sample due to a high degree of disorder, there is evidence that Pu is strongly bound to the ferrihydrite solids through a combination of adsorption and/or coprecipitation as evidenced by the high number of Pu-Fe scatterers. In these sample a fraction of Pu could coprecipitate with ferrihydrite and/or form a inner sphere complex with multiple Fe sites. The EXAFS data show that the Pu binding site changes significantly during ferrihydrite transformation to goethite, indicating that Pu is mobilized during hydrothermal alteration; however, only a small fraction of Pu in the highest Pu concentration samples (G-FHc-3000) is remobilized to form PuO_2. In all goethite samples Pu is

strongly sorbed (either coprecipitated and/or adsorbed as inner sphere complex) to the goethite as evidenced by the presence of Pu-Fe scatterers. The acid leaching results support this conclusion by showing that less Pu is accessible to leaching in goethite formed via coprecipitation process, compared to the goethite formed via the sorption process. These observations confirm that the nature of Pu associated with the mineral will affect the leachability of Pu from the solids and suggests that a fraction of the Pu may be incorporated into the goethite structure either in a distorted Fe crystallographic position or may coprecipitate as a separate phase.

Implications for the natural and engineered environment

Our results show that variations in the synthetic routes (sorption vs. coprecipitation) of ferrihydrite at pH ~8 impact the nature of Pu associated with the mineral. The major difference between the two synthetic processes is the timing of Pu addition to the ferrihydrite precipitate and we expect both processes to be of environmental relevance. For example, the sorption method, where Pu is added at pH ~8 to an already formed ferrihydrite, simulates a simple scenario where Pu becomes associated with a preexisting mineral substrate. In the coprecipitation method a Pu-ferrihydrite precipitate is formed from neutralizing the pH of an acidic solution containing dissolved Pu and Fe. This synthetic method likely simulates a scenario where an acidic plume is neutralized for remediation purposes or where changes in geochemical conditions occur in contaminated streams or ponds (e.g. the Mayak site [84]). Secondary iron (oxy)hydroxides with associated Pu and other radionuclides have been identified in surface contaminated waters in a pH range of 5.9-8.2 [59, 61, 85] and although the mechanisms of formation of these radioactive particles is still unclear, both sorption and secondary mineral formation processes are likely involved . [59, 61, 85]

Our results also show that differences that exist in the Pu association with the precursor material are retained through transformation to goethite. The hydrothermal alteration to goethite however was conducted in the alkaline to hyperalkaline pH range (~10-11). Many underground repository concepts utilize cementitious materials in the design as part of the engineered barrier system or as structural materials. [86] The pH during leaching of these materials upon resaturation will buffer to hyperalkaline conditions (pH 10.5−13.1), creating a plume of alkaline fluid in the host rock and/or local environment. [86] Furthermore, hyperalkaline conditions can prevail in many contaminated land scenarios, e.g., where cementitious building materials contact subsurface sediments [87, 88] and at the underground waste storage tanks at the Hanford Site in Washington State, USA. [89]

Overall the results presented in this study provide valuable new insights into Pu(IV)- iron (oxy)hydroxide interactions in the natural and engineered environment and highlight the importance of understanding the fate of radionuclides during mineral phase transformation processes.

Acknowledgments

Work at Lawrence Livermore National Laboratory was performed with funding from the Spent Fuel and Waste Science and Technology campaign of the U.S. Department of Energy's Nuclear Energy Program and the Department of Energy, Office of Science, Biological and Environmental Research, Subsurface Biogeochemical Research program (SCW1053) and performed under the auspices of the U.S. Department of Energy by Lawrence Livermore National Laboratory under Contract DE-AC52-07NA27344. Work at Lawrence Berkeley National Laboratory was supported by the Department of Energy, Office of Science, Biological and Environmental Research, Subsurface Biogeochemical Research program (SCW1053) under a subcontract with Lawrence Livermore National Laboratory. EXAFS measurements were performed at beamlines 11-2 at the

Stanford Synchrotron Radiation Lightsource, which is supported by the U.S. Department of Energy, Office of Science, Office of Basic Energy Sciences under contract no. DE-AC02-76SF00515. LLNL-JRNL-812443

Supporting Information

The following files are available free of charge. Supplementary figures (.docx) Figure SI 1: TEM and STEM images of FHc-3000 (a. and b.) and of G-FHc-3000 (c.d.); Figure SI 2: Concentration of Pu measured via liquid scintillation counting for supernatant, first and second rinse. Data shown with 2σ error bars. The percentage of Pu remaining in the supernatant is < 0.2 ± 0.08 % for G-FHs-1000, G-FHs-3000, G-FHc-1000, and G-FHc-3000, whereas for G-FHs-400 and G-FHc-400 it ranged between 0.6-0.8%.Figure SI 3: Leaching behavior of Pu (%) in acidic solution (0.001-4M) for G-FHs-3000 (black: centrifuged supernatant; gray: filtered with 3kDa ultrafiltration device) and G-FHc-3000 (dark blu: centrifuged supernatant; light blu: filtered with 3kDa ultrafiltration device). Data shown with 2σ error bars; Figure SI 4 2: Leaching behavior of Fe in acidic solution (0.001-4 M) for Pu-free goethite; Figure SI 5. Pu L_{III}-edge XANES spectra collected from Pu-ferrihydrite / Pu-goethite samples in this study. The spectra were calibrated to the Zr K edge at 17995.88 eV. [1] Edge inflection points (see Table SI 1) all fall within the range of those determined by Conradson et al., 2004 [2] for a range of Pu(IV) solid phases confirming Pu(IV) as the predominant oxidation state in our samples.; Figure SI 6: Average Pu coordination number with respect to particle size in PuO_2 solids as calculated using Calvin analysis[90].; Table SI 1. Edge inflection point (edge energy, E_0) of Pu-ferrihydrite / Pu-goethite samples in this study.; Table SI 2. Alternative EXAFS fits for FH-S-3000.

References

1. Choppin, G. R., Redox speciation of plutonium in natural waters. *Journal of Radioanalytical and Nuclear Chemistry-Articles* **1991,** *147* (1), 109-116.
2. Sanchez, A. L.; Murray, J. W.; Sibley, T. H., The adsorption of plutonium IV and V on goethite. *Geochimica et Cosmochimica Acta* **1985,** *49* (11), 2297-2307.
3. Begg, J. D.; Edelman, C.; Zavarin, M.; Kersting, A. B., Sorption kinetics of plutonium (V)/(VI) to three montmorillonite clays. *Applied Geochemistry* **2018,** *96*, 131-137.
4. Efurd, D. W.; Runde, W.; Banar, J.; Janecky, D.; Kaszuba, J.; Palmer, P.; Roensch, F.; Tait, C. D., Neptunium and Plutonium Solubilities in a Yucca Mountain Groundwater. *Environmental science technology* **1998,** *32* (24), 3893-3900.
5. Neck, V.; Altmaier, M.; Seibert, A.; Yun, J. I.; Marquardt, C. M.; Fanghaenel, T., Solubility and redox reactions of Pu(IV) hydrous oxide: Evidence for the formation of PuO2+x(s, hyd). *Radiochimica Acta* **2007,** *95* (4), 193-207.
6. Zhao, P. H.; Zavarin, M.; Leif, R. N.; Powell, B. A.; Singleton, M. J.; Lindvall, R. E.; Kersting, A. B., Mobilization of actinides by dissolved organic compounds at the Nevada Test Site. *Applied Geochemistry* **2011,** *26* (3), 308-318.
7. Icopini, G. A.; Lack, J. G.; Hersman, L. E.; Neu, M. P.; Boukhalfa, H., Plutonium(V/VI) Reduction by the Metal-Reducing Bacteria Geobacter metallireducens GS-15 and Shewanella oneidensis MR-1. *Applied and Environmental Microbiology* **2009,** *75* (11), 3641-3647.
8. Powell, B. A.; Fjeld, R. A.; Kaplan, D. I.; Coates, J. T.; Serkiz, S. M., $Pu(V)O_2^+$ adsorption and reduction by synthetic magnetite (Fe_3O_4). *Environmental Science & Technology* **2004,** *38* (22), 6016-6024.
9. Zavarin, M.; Powell, B. A.; Bourbin, M.; Zhao, P.; Kersting, A. B., Np(V) and Pu(V) Ion Exchange and Surface-Mediated Reduction Mechanisms on Montmorillonite. *Environ. Sci. Technol.* **2012,** *46* (5), 2692-2698.
10. Begg, J. D.; Zavarin, M.; Kersting, A. B., Desorption of plutonium from montmorillonite: An experimental and modeling study. *Geochimica Et Cosmochimica Acta* **2017,** *197*, 278-293.
11. Choppin, G. R., Solution chemistry of the actinides. *Radiochimica Acta* **1983,** *32* (1-3), 43-53.
12. Clark, D. L.; Hobart, D. E.; Neu, M. P., Actinide Carbonate Complexes and their Importance in Actinide Environmental Chemistry. *Chemical reviews* **1995,** *95* (1), 25-48.
13. Maher, K.; Bargar, J. R.; Brown, G. E., Jr., Environmental Speciation of Actinides. *Inorganic chemistry* **2013,** *52* (7), 3510-3532.
14. Begg, J. D.; Zavarin, M.; Tumey, S. J.; Kersting, A. B., Plutonium sorption and desorption behavior on bentonite. *Journal of Environmental Radioactivity* **2015,** *141*, 106-114.
15. Powell, B. A.; Dai, Z. R.; Zavarin, M.; Zhao, P. H.; Kersting, A. B., Stabilization of Plutonium Nano-Colloids by Epitaxial Distortion on Mineral Surfaces. *Environmental Science & Technology* **2011,** *45* (7), 2698-2703.
16. Dalodiere, E.; Virot, M.; Morosini, V.; Chave, T.; Dumas, T.; Hennig, C.; Wiss, T.; Blanco, O. D.; Shuh, D. K.; Tyliszcak, T.; Venault, L.; Moisy, P.; Nikitenko, S. I., Insights

into the sonochemical synthesis and properties of salt-free intrinsic plutonium colloids. *Scientific Reports* **2017,** *7*.
17. Gerber, E.; Romanchuk, A. Y.; Pidchenko, I.; Amidani, L.; Rossberg, A.; Hennig, C.; Vaughan, G. B. M.; Trigub, A.; Egorova, T.; Bauters, S.; Plakhova, T.; Hunault, M. O. J. Y.; Weiss, S.; Butorin, S. M.; Scheinost, A. C.; Kalmykov, S. N.; Kvashnina, K. O., The missing pieces of the PuO2 nanoparticle puzzle. *Nanoscale* **2020**.
18. Micheau, C.; Virot, M.; Dourdain, S.; Dumas, T.; Menut, D.; Solari, P. L.; Venault, L.; Diat, O.; Moisy, P.; Nikitenko, S. I., Relevance of formation conditions to the size, morphology and local structure of intrinsic plutonium colloids. *Environmental Science: Nano* **2020**.
19. Moreau, L. M.; Herve, A.; Straub, M. D.; Russo, D. R.; Abergel, R. J.; Alayoglu, S.; Arnold, J.; Braun, A.; Deblonde, G. J. P.; Liu, Y.; Lohrey, T. D.; Olive, D. T.; Qiao, Y.; Rees, J. A.; Shuh, D. K.; Teat, S. J.; Booth, C. H.; Minasian, S. G., Structural properties of ultra-small thorium and uranium dioxide nanoparticles embedded in a covalent organic framework. *Chemical Science* **2020,** *11* (18), 4648-4668.
20. Begg, J. D.; Zavarin, M.; Zhao, P.; Tumey, S. J.; Powell, B.; Kersting, A. B., Pu(V) and Pu(IV) Sorption to Montmorillonite. *Environmental Science & Technology* **2013,** *47* (10), 5146-5153.
21. Hixon, A. E.; Hu, Y. J.; Kaplan, D. I.; Kukkadapu, R. K.; Nitsche, H.; Qafoku, O.; Powell, B. A., Influence of iron redox transformations on plutonium sorption to sediments. *Radiochimica Acta* **2010,** *98* (9-11), 685-692.
22. Kirsch, R.; Fellhauer, D.; Altmaier, M.; Neck, V.; Rossberg, A.; Fanghanel, T.; Charlet, L.; Scheinost, A. C., Oxidation state and local structure of plutonium reacted with magnetite, mackinawite, and chukanovite. *Environmental Science & Technology* **2011,** *45* (17), 7267-7274.
23. Shaughnessy, D. A.; Nitsche, H.; Booth, C. H.; Shuh, D. K.; Waychunas, G. A.; Wilson, R. E.; Gill, H.; Cantrell, K. J.; Serne, R. J., Molecular interfacial reactions between Pu(VI) and manganese oxide minerals manganite and hausmannite. *Environmental Science & Technology* **2003,** *37* (15), 3367-3374.
24. Zhao, P. H.; Begg, J. D.; Zavarin, M.; Tumey, S. J.; Williams, R.; Dai, Z. R. R.; Kips, R.; Kersting, A. B., Plutonium(IV) and (V) Sorption to Goethite at Sub-Femtomolar to Micromolar Concentrations: Redox Transformations and Surface Precipitation. *Environmental Science & Technology* **2016,** *50* (13), 6948-6956.
25. Romanchuk, A. Y.; Kalmykov, S. N.; Aliev, R. A., Plutonium sorption onto hematite colloids at femto- and nanomolar concentrations. *Radiochimica Acta* **2011,** *99* (3), 137-144.
26. Marshall, T. A.; Morris, K.; Law, G. T. W.; Livens, F. R.; Mosselmans, J. F. W.; Bots, P.; Shaw, S., Incorporation of Uranium into Hematite during Crystallization from Ferrihydrite. *Environmental Science & Technology* **2014,** *48* (7), 3724-3731.
27. Ferris, F. G.; Hallberg, R. O.; Lyven, B.; Pedersen, K., Retention of strontium, cesium, lead and uranium by bacterial iron oxides from a subterranean environment. *Applied Geochemistry* **2000,** *15* (7), 1035-1042.
28. Alberts, J. J.; Halverson, J. E.; Orlandini, K. A., The Distribution of Plutonium, Americium and Curium Isotopes in Pond and Stream Sediments of the Savannah River Plant, South-Carolina, USA. *Journal of Environmental Radioactivity* **1986,** *3* (4), 249-271.

29. Pinder, J. E.; Alberts, J. J.; Bowling, J. W.; Nelson, D. M.; Orlandini, K. A., The annual cycle of plutonium in the water column of a warm, monomictic reservoir. *Journal of Environmental Radioactivity* **1992,** *17* (1), 59-81.
30. Whicker, F. W.; Pinder, J. E.; Bowling, J. W.; Alberts, J. J.; Brisbin, I. L., Distribution of long-lived radionuclides in an abandoned reactor cooling reservoir. *Ecological Monographs* **1990,** *60* (4), 471-496.
31. Benner, S. G.; Hansel, C. M.; Wielinga, B. W.; Barber, T. M.; Fendorf, S., Reductive dissolution and biomineralization of iron hydroxide under dynamic flow conditions. *Environmental Science & Technology* **2002,** *36* (8), 1705-1711.
32. Luther, G. W.; Kostka, J. E.; Church, T. M.; Sulzberger, B.; Stumm, W., Seasonal Iron Cycling in the Salt-Marsh Sedimentary Environment - the Importance of Ligand Complexes with Fe(II) and Fe(III) in the Dissolution of Fe(III) Minerals and Pyrite, Respectively. *Marine Chemistry* **1992,** *40* (1-2), 81-103.
33. King, F., 13 - Nuclear waste canister materials: Corrosion behavior and long-term performance in geological repository systems. In *Geological Repository Systems for Safe Disposal of Spent Nuclear Fuels and Radioactive Waste (Second Edition)*, Apted, M. J.; Ahn, J., Eds. Woodhead Publishing: 2017; pp 365-408.
34. Feron, D.; Crusset, D.; Gras, J. M., Corrosion issues in nuclear waste disposal. *Journal of Nuclear Materials* **2008,** *379* (1-3), 16-23.
35. Music, S.; Gotic, M.; Popovic, S., X-Ray-Diffraction and Fourier-Transform Infrared-Analysis of the Rust Formed by Corrosion of Steel in Aqueous-Solutions. *Journal of Materials Science* **1993,** *28* (21), 5744-5752.
36. El Hajj, H.; Abdelouas, A.; El Mendili, Y.; Karakurt, G.; Grambow, B.; Martin, C., Corrosion of carbon steel under sequential aerobic-anaerobic environmental conditions. *Corrosion Science* **2013,** *76*, 432-440.
37. Wersin, P.; Jenni, A.; Mader, U. K., Interaction of Corroding Iron with Bentonite in the Abm1 Experiment at Aspo, Sweden: A Microscopic Approach. *Clays and Clay Minerals* **2015,** *63* (1-2), 51-68.
38. Michel, F. M.; Ehm, L.; Antao, S. M.; Lee, P. L.; Chupas, P. J.; Liu, G.; Strongin, D. R.; Schoonen, M. A. A.; Phillips, B. L.; Parise, J. B., The Structure of Ferrihydrite, a Nanocrystalline Material. *Science* **2007,** *316* (5832), 1726-1729.
39. Fischer, W. R.; Schwertmann, U., Formation of hematite from amorphous iron(III)hydroxide. *Clays and Clay Minerals* **1975,** *23* (1), 33-39.
40. Combes, J. M.; Manceau, A.; Calas, G., Formation Of Ferric Oxides From Aqueous-Solutions - A Polyhedral Approach By X-Ray Absorption-Spectroscopy. *Geochimica Et Cosmochimica Acta* **1990,** *54* (4), 1083-1091.
41. Schwertmann, U.; Cornell, R. M., Iron oxides in the laboratory. In *Iron Oxides in the Laboratory*, Wiley-VCH Verlag GmbH: 2000; pp i-xviii.
42. Das, S.; Hendry, M. J.; Essilfie-Dughan, J., Transformation of Two-Line Ferrihydrite to Goethite and Hematite as a Function of pH and Temperature. *Environmental Science & Technology* **2011,** *45* (1), 268-275.
43. Shaw, S.; Pepper, S. E.; Bryan, N. D.; Livens, F. R., The kinetics and mechanisms of goethite and hematite crystallization under alkaline conditions, and in the presence of phosphate. *American Mineralogist* **2005,** *90* (11-12), 1852-1860.

44. Ray, J. R.; Wan, W.; Gilbert, B.; Jun, Y. S., Effects of Formation Conditions on the Physicochemical Properties, Aggregation, and Phase Transformation of Iron Oxide Nanoparticles. *Langmuir* **2013,** *29* (4), 1069-1076.
45. Yang, R.; Tao, J.; Huang, Q.; Tie, B.; Lei, M.; Yang, Y.; Du, H., Co-adsorption of Cd(II) and Sb(III) by ferrihydrite: a combined XPS and ITC study. *Journal of Soils and Sediments* **2019,** *19* (3), 1319-1327.
46. Dyer, J. A.; Trivedi, P.; Scrivner, N. C.; Sparks, D. L., Lead Sorption onto Ferrihydrite. 2. Surface Complexation Modeling. *Environmental Science & Technology* **2003,** *37* (5), 915-922.
47. Jain, A.; Loeppert, R. H., Effect of Competing Anions on the Adsorption of Arsenate and Arsenite by Ferrihydrite. *Journal of Environmental Quality* **2000,** *29*, 1422-1430.
48. Smith, K. F.; Morris, K.; Law, G. T. W.; Winstanley, E. H.; Livens, F. R.; Weatherill, J. S.; Abrahamsen-Mills, L. G.; Bryan, N. D.; Mosselmans, J. F. W.; Cibin, G.; Parry, S.; Blackham, R.; Law, K. A.; Shaw, S., Plutonium(IV) Sorption during Ferrihydrite Nanoparticle Formation. *ACS Earth and Space Chemistry* **2019**.
49. Bots, P.; Shaw, S.; Law, G. T. W.; Marshall, T. A.; Mosselmans, J. F. W.; Morris, K., Controls on the Fate and Speciation of Np(V) During Iron (Oxyhydr)oxide Crystallization. *Environmental Science & Technology* **2016,** *50* (7), 3382-3390.
50. Um, W.; Serne, R. J.; Brown, C. F.; Rod, K. A., Uranium(VI) sorption on iron oxides in Hanford Site sediment: Application of a surface complexation model. *Applied Geochemistry* **2008,** *23* (9), 2649-2657.
51. Romanchuk, A. Y.; Gusev, I. V.; Vlasova, I. E.; Petrov, V. G.; Kuzmenkova, N. V.; Egorova, B. V.; Zakharova, E. V.; Volkova, A. G.; Kalmykov, S. N., Interaction of Plutonium with Iron- and Chromium-Containing Precipitates under the Conditions of Reservoir Bed for Liquid Radioactive Waste. *Radiochemistry* **2016,** *58* (6), 662-667.
52. Sylvester, P.; Milner, T.; Jensen, J., Radioactive liquid waste treatment at Fukushima Daiichi. *Journal of Chemical Technology and Biotechnology* **2013,** *88* (9), 1592-1596.
53. Winstanley, E. H.; Morris, K.; Abrahamsen-Mills, L. G.; Blackham, R.; Shaw, S., U(VI) sorption during ferrihydrite formation: Underpinning radioactive effluent treatment. *Journal of Hazardous Materials* **2019,** *366*, 98-104.
54. McBriarty, M. E.; Soltis, J. A.; Kerisit, S.; Qafoku, O.; Bowden, M. E.; Bylaska, E. J.; De Yoreo, J. J.; Ilton, E. S., Trace Uranium Partitioning in a Multiphase Nano-FeOOH System. *Environmental Science & Technology* **2017,** *51* (9), 4970-4977.
55. Zavarin, M.; Zhao, P.; Dai, Z.; Kersting Annie , B., Plutonium sorption and precipitation in the presence of goethite at 25 and 80 ○C. In *Radiochimica Acta*, 2014; Vol. 102, p 983.
56. Felmy, A. R.; Moore, D. A.; Qafoku, O.; Buck, E.; Conradson, S. D.; Ilton, E. S., Heterogeneous reduction of (PuO2)-Pu-239 by aqueous Fe(II) in the presence of hematite. *Radiochimica Acta* **2013,** *101* (11), 701-710.
57. Dumas, T.; Fellhauer, D.; Schild, D.; Gaona, X.; Altmaier, M.; Scheinost, A. C., Plutonium Retention Mechanisms by Magnetite under Anoxic Conditions: Entrapment versus Sorption. *Acs Earth and Space Chemistry* **2019,** *3* (10), 2197-2206.
58. Joseph, C.; Balboni, E.; Baumer, T.; Treinen, K.; Kersting, A. B.; Zavarin, M., Plutonium Desorption from Nuclear Melt Glass-Derived Colloids and Implications for Migration at the Nevada National Security Site, USA. *Environmental Science & Technology* **2019,** *53* (21), 12238-12246.

59. Novikov, A. P.; Kalmykov, S. N.; Utsunomiya, S.; Ewing, R. C.; Horreard, F.; Merkulov, A.; Clark, S. B.; Tkachev, V. V.; Myasoedov, B. F., Colloid transport of plutonium in the far-field of the Mayak Production Association, Russia. *Science* **2006,** *314* (5799), 638-641.
60. Batuk, O. N.; Conradson, S. D.; Aleksandrova, O. N.; Boukhalfa, H.; Burakov, B. E.; Clark, D. L.; Czerwinski, K. R.; Felmy, A. R.; Lezama-Pacheco, J. S.; Kalmykov, S. N.; Moore, D. A.; Myasoedov, B. F.; Reed, D. T.; Reilly, D. D.; Roback, R. C.; Vlasova, I. E.; Webb, S. M.; Wilkerson, M. P., Multiscale Speciation of U and Pu at Chernobyl, Hanford, Los Alamos, McGuire AFB, Mayak, and Rocky Flats. *Environmental Science & Technology* **2015,** *49* (11), 6474-6484.
61. Lukashenko, S.; Kabdyrakova, A.; Lind, O. C.; Gorlachev, I.; Kunduzbayeva, A.; Kvochkina, T.; Janssens, K.; De Nolf, W.; Yakovenko, Y.; Salbu, B., Radioactive particles released from different sources in the Semipalatinsk Test Site. *Journal of Environmental Radioactivity* **2020,** *216*.
62. Joshi, S. R., Lanthanum fluoride coprecipitation techniques for the preparation of actinides for alpha-spectrometry. *Journal of Radioanalytical and Nuclear Chemistry* **1985,** *90* (2), 409-414.
63. Hayes, T. M.; Boyce, J. B., Extended X-Ray Absorption Fine Structure Spectroscopy. In *Solid State Physics*, Ehrenreich, H.; Seitz, F.; Turnbull, D., Eds. Academic Press: 1983; Vol. 37, pp 173-351.
64. Booth, C. H. *RSXAP EXAFS Analysis Package*.
65. Li, G. G.; Bridges, F.; Booth, C. H., X-ray absorption fine-structure standards - A comparison of experiment and theory. *Physical Review B* **1995,** *52* (9), 6332-6348.
66. Ankudinov, A. L.; Ravel, B.; Rehr, J. J.; Conradson, S. D., Real-space multiple-scattering calculation and interpretation of x-ray-absorption near-edge structure. *Physical Review B* **1998,** *58* (12), 7565-7576.
67. Booth, C. H.; Hu, Y. J., Confirmation of standard error analysis techniques applied to EXAFS using simulations. *In Proceedings of 14th International Conference on X-Ray Absorption Fine Structure (XAFS14)* **2009,** *190*.
68. Wyckoff, R. W. G., *Crystal Structures*. Interscience Publishers, New York: 1963.
69. Wylie, E. M.; Olive, D. T.; Powell, B. A., Effects of Titanium Doping in Titanomagnetite on Neptunium Sorption and Speciation. *Environmental Science & Technology* **2016,** *50* (4), 1853-1858.
70. Romanchuk, A. Y.; Kalmykov, S. N.; Egorov, A. V.; Zubavichus, Y. V.; Shiryaev, A. A.; Batuk, O. N.; Conradson, S. D.; Pankratov, D. A.; Presnyakov, I. A., Formation of crystalline PuO2+x・nH(2)O nanoparticles upon sorption of Pu(V,VI) onto hematite. *Geochimica Et Cosmochimica Acta* **2013,** *121*, 29-40.
71. Hu, Y.-J.; Kestrel Schwaiger, L.; Booth Corwin, H.; Kukkadapu Ravi, K.; Cristiano, E.; Kaplan, D.; Nitsche, H., Molecular interactions of plutonium(VI) with synthetic manganese-substituted goethite. In *Radiochimica Acta International journal for chemical aspects of nuclear science and technology*, 2010; Vol. 98, p 655.
72. Bargar, J. R.; Reitmeyer, R.; Lenhart, J. J.; Davis, J. A., Characterization of U(VI)-carbonato ternary complexes on hematite: EXAFS and electrophoretic mobility measurements. *Geochimica Et Cosmochimica Acta* **2000,** *64* (16), 2737-2749.
73. Seco, F.; Hennig, C.; de Pablo, J.; Rovira, M.; Rojo, I.; Marti, V.; Gimenez, J.; Duro, L.; Grive, M.; Bruno, J., Sorption of Th(IV) onto Iron Corrosion Products: EXAFS Study. *Environmental Science & Technology* **2009,** *43* (8), 2825-2830.

74. Dumas, T.; Guigue, M.; Moisy, P.; Colina-Ruiz, R.; de Leon, J. M.; Matara-Aho, M.; Solari, P. L.; Monfort, M.; Moulin, C.; Beccia, M. R.; Den Auwer, C., Experimental Speciation of Plutonium(IV) in Natural Seawater. *Chemistryselect* **2018,** *3* (7), 2021-2024.
75. Shannon, R. D., Revised Effective Ionic-Radii and Systematic Studies of Interatomic Distances in Halides and Chalcogenides. *Acta Crystallographica Section A* **1976,** *32* (Sep1), 751-767.
76. Wang, X.; Zhu, M.; Koopal, L. K.; Li, W.; Xu, W.; Liu, F.; Zhang, J.; Liu, Q.; Feng, X.; Sparks, D. L., Effects of crystallite size on the structure and magnetism of ferrihydrite. *Environmental Science: Nano* **2016,** *3* (1), 190-202.
77. Siroux, B.; Beaucaire, C.; Tabarant, M.; Benedetti, M. F.; Reiller, P. E., Adsorption of strontium and caesium onto an Na-MX80 bentonite: Experiments and building of a coherent thermodynamic modelling. *Applied Geochemistry* **2017,** *87* (Supplement C), 167-175.
78. Vila, F. D.; Rehr, J. J.; Rossner, H. H.; Krappe, H. J., Theoretical x-ray absorption Debye-Waller factors. *Physical Review B* **2007,** *76* (1).
79. Stefansson, A., Iron(III) hydrolysis and solubility at 25 degrees C. *Environmental Science & Technology* **2007,** *41* (17), 6117-6123.
80. Cornell, R. M.; Giovanoli, R.; Schneider, W., Review of the hydrolysis of Fe(III) and the crystallization of amorphous Fe(III) hydroxide hydrate. *Journal of Chemical Technology and Biotechnology* **1989,** *46* (2), 115-134.
81. Downward, L.; Booth, C. H.; Lukens, W. W.; Bridges, F., A variation of the F-Test for determining statistical relevance of particular parameters in EXAFS fits. *X-Ray Absorption Fine Structure-Xafs13* **2007,** *882*, 129-+.
82. Kaur, N.; Grafe, M.; Singh, B.; Kennedy, B., Simultaneous incorporation of Cr, Zn, Cd and Pb in the goethite structure. *Clays and Clay Minerals* **2009,** *57* (2), 234-250.
83. Yang, H. X.; Lu, R.; Downs, R. T.; Costin, G., Goethite, alpha-FeO(OH), from single-crystal data. *Acta Crystallographica Section E-Structure Reports Online* **2006,** *62*, I250-I252.
84. *Sources contributing to radioactive contamination of the Techa river and areas surrounding the Mayak production association, Urals, Russia* http://inis.iaea.org/search/search.aspx?orig_q=RN:29032387; 82-993079-6-1; Statens Straalevern, Oesteraas: Norway, 1997; p 142.
85. Toropov, A. S., Migration Forms of Anthropogenic Radionuclides in Tunnel Waters at the Degelen Mountains, Semipalatinsk Test Site. *Geochemistry International* **2020,** *58* (3), 342-351.
86. Berner, U. R., Evolution of pore water chemistry during degradation of cement in a radioactive waste repository environment. *Waste Management* **1992,** *12* (2), 201-219.
87. Wallace, S. H.; Shaw, S.; Morris, K.; Small, J. S.; Burke, I. T., Alteration of Sediments by Hyperalkaline K-Rich Cement Leachate: Implications for Strontium Adsorption and Incorporation. *Environmental Science & Technology* **2013,** *47* (8), 3694-3700.
88. Wallace, S. H.; Shaw, S.; Morris, K.; Small, J. S.; Fuller, A. J.; Burke, I. T., Effect of groundwater pH and ionic strength on strontium sorption in aquifer sediments: Implications for Sr-90 mobility at contaminated nuclear sites. *Applied Geochemistry* **2012,** *27* (8), 1482-1491.
89. Deng, Y.; Harsh, J. B.; Flury, M.; Young, J. S.; Boyle, J. S., Mineral formation during simulated leaks of Hanford waste tanks. *Applied Geochemistry* **2006,** *21* (8), 1392-1409.
90. Calvin, S.; Riedel, C. J.; Carpenter, E. E.; Morrison, S. A.; Stroud, R. M.; Harris, V. G., Estimating crystallite size in polydispersed samples using EXAFS. *Physica Scripta* **2005,** *T115*, 744-748.